



***Operando* video microscopy of Li plating and re-intercalation on graphite anodes during fast charging**

Journal:	<i>Journal of Materials Chemistry A</i>
Manuscript ID	TA-ART-07-2021-006023.R1
Article Type:	Paper
Date Submitted by the Author:	10-Sep-2021
Complete List of Authors:	Chen, Yuxin; University of Michigan, Mechanical Engineering Chen, Kuan-Hung; University of Michigan, Materials Science and Engineering Sanchez, Adrian; University of Michigan, Mechanical Engineering Kazyak, Eric; University of Michigan, Mechanical Engineering Goel, Vishwas; University of Michigan, Materials Science & Engineering Gorlin, Yelena; Robert Bosch LLC Research and Technology Center North America, Energy Technologies Christensen, Jake; Robert Bosch LLC Thornton, Katsuyo; University of Michigan, ; Dasgupta, Neil; University of Michigan, Mechanical Engineering

***Operando* video microscopy of Li plating and re-intercalation on graphite anodes during fast charging**

Yuxin Chen¹, Kuan-Hung Chen², Adrian J. Sanchez¹, Eric Kazyak¹, Vishwas Goel², Yelena Gorlin³, Jake Christensen³, Katsuyo Thornton², Neil P. Dasgupta^{1,2*}

¹ Department of Mechanical Engineering, University of Michigan, Ann Arbor, MI 48109, USA

² Department of Materials Science & Engineering, University of Michigan, Ann Arbor, MI 48109, USA

³ Robert Bosch LLC, Research and Technology Center, Sunnyvale, CA 94085, USA

*Corresponding Author: ndasgupt@umich.edu

KEYWORDS Lithium-ion battery, Lithium plating, fast charging, *Operando* microscopy, heterogeneity

ABSTRACT

Despite the demand for fast-charging Lithium (Li)-ion batteries, high-energy-density batteries with thick graphite anodes are limited by Li plating when charging at $>4C$ rates. In this work, plan-view *operando* video microscopy is applied on >3 mAh cm⁻² calendared graphite electrodes to study the dynamic evolution of local state-of-charge (SoC) and Li plating during fast charging. This technique allows for visualization of the spatial heterogeneity in SoC across the electrode, nucleation and growth of Li filaments, Li re-intercalation into graphite, “dead Li” formation, and SoC equilibration. The *operando* microscopy analysis is complimented by *ex situ* imaging of through-plane gradients in SoC to gain a 3-dimensional visualization of spatial heterogeneity. We demonstrate that (1) Li plating preferentially nucleates on the graphite particles that lithiate fastest during fast charging; (2) the onset of Li plating correlates with the local minimum of the graphite electrode potential; (3) galvanic corrosion currents are responsible for Li re-intercalation, dead Li formation, and SoC re-equilibration after fast charging; and (4) electrochemical signatures during OCV rest or discharge are associated with Li re-intercalation into graphite. This work provides insight into the Li-

graphite interactions at the composite electrode level and can be used to inform strategies to diagnose and mitigate Li plating during fast charging.

INTRODUCTION

Li-ion batteries (LIBs) have enabled significant advances in portable energy storage, and their demand is projected to increase greatly due to the growing market for electric vehicles ¹. The desire to improve energy density and decrease cost has motivated an increase in the areal capacity of the electrodes (>3 mAh cm⁻²). However, as electrode thickness increases, mass transport limitations become increasingly important ², and the performance of high-energy-density LIBs becomes limited at high charge rates (<15 minute charge).

During charging, Li ions intercalate into the graphite electrode according to the following reaction:



The reversible potential of lithiated graphite at $0.5 \leq x \leq 1$ is less than 100 mV more positive than the equilibrium Li/Li⁺ potential ³. This increases the risk of metallic Li plating during fast charging, since the electrochemical potential of graphite can drop to values more negative than Li/Li⁺, where Li plating becomes thermodynamically favorable:



The Li plating reaction is often triggered under fast-charging conditions, which is a consequence of cell polarization that arises from mass transport limitations, ohmic resistance, and/or charge transfer kinetics ². Li plating can cause capacity loss, electrolyte consumption, gas evolution, internal electrical shorting, and thermal runaway ⁴⁻⁶.

Although Li plating is regarded as a harmful side reaction in graphite batteries, a fraction of the plated Li capacity can be recovered. Depending on the cycling protocol, this recovery can occur during the constant voltage (CV) charge period after constant current (CC) charging, during the discharge half cycle, or during open circuit voltage (OCV) rest periods ^{7,8,17,9-16}. During the recovery process, portions of the

plated Li can become disconnected (and/or kinetically restricted) from the graphite, resulting in the formation of “dead Li”^{7,8,10,12–15,17}. It has been previously shown that the isolated (inactive) metallic Li that remains on the graphite surface is a substantial source of irreversible capacity loss during 4C charging, which can be differentiated from SEI growth using mass spectrometry titration¹⁸.

To gain an improved fundamental understanding of these processes, Li plating on graphite has been studied a wide range of *in situ* techniques, including acoustic ultrasound¹⁹, nuclear magnetic resonance (NMR) spectroscopy^{12–15,20}, neutron diffraction^{9,11}, electron paramagnetic resonance (EPR) spectroscopy⁷, optical microscopy^{8,10,21,22}, X-ray diffraction (XRD) and tomography^{16,23,24}, and mass spectrometry²⁵. Moreover, a variety of analytical electrochemistry methods have been used to detect Li plating, including high-precision Coulometry²⁶, three-electrode measurements²⁷ and differential voltage analysis^{27–32}.

After Li plating has occurred during a fast-charge step, a subsequent decrease in the metallic Li signal has been detected during the OCV rest and discharge steps using *in situ* NMR^{14,20}. An analogous decrease in the Li signal was observed during the CV portion of a 6C charging step via *operando* synchrotron XRD¹⁶. Additionally, *in situ* neutron diffraction has been applied at sub-ambient temperatures during OCV rests after charging^{9,11}. An increase was observed in the LiC₆ phase, along with a corresponding decrease in LiC₁₂, which was attributed to the re-intercalation of Li⁺ into graphite from the plated Li. To quantify the amount of dead Li formed during OCV and discharge, *operando* EPR spectroscopy was performed⁷.

Although fast charging is highly relevant for many applications, it remains challenging to directly capture the dynamic evolution of Li plating. At room temperature, the nucleation and growth behavior of plated Li evolves rapidly, and therefore a temporal resolution on the order of seconds is needed to capture these dynamic changes⁸. However, in order to observe the metallic Li signal, it requires more than one minute to perform a scan using NMR, EPR or XRD^{7,14,16}. Even when performing synchrotron XRD, the relatively weak diffraction signal for metallic Li requires for multiple scans to be binned across multiple spatial and temporal points to reduce the impact of noise¹⁶, and thus reduces the spatial and temporal resolution.

Alternatively, optical microscopy is capable of probing the dynamics of fast charging at room temperature with reduced tradeoffs in spatiotemporal resolution. 2-D images can be captured at rates of less than 1 second per frame with a spatial resolution of $\sim 1 \mu\text{m}$. For 3-D focal series reconstructions, which are used in this work, $\sim 15\text{-}20$ seconds per frame is achievable without decreasing the spatial resolution and maintaining a wide field of view. Previous reports of *in situ* optical microscopy have observed Li plating after fast charging^{8,17} and after extensive charging at low rates^{10,22,33}. For example, Guo et al. overcharged graphite at 0.2C and observed Li dendrites at the edge of the electrode¹⁰. Harris et al. observed sparse Li plating during a CV hold²². *Operando* optical microscopy has also been applied to observe the disappearance of a portion of the plated Li on calendared electrodes⁸ and on individual highly oriented pyrolytic graphite (HOPG) particles¹⁷.

Despite the progress in *in situ/operando* analysis of Li plating on graphite, there have been a limited number of reports that synchronize the morphological evolution of the system with its voltage response^{7,9,11,16,17}. Such time-resolved studies allow for a detailed mechanistic understanding of the electrochemical signatures associated with the interactions between plated Li and graphite. Furthermore, for the analysis to be relevant for practical batteries, it is important to use graphite electrodes with relevant thickness and porosity. Additionally, in order to avoid artefacts from current focusing (such preferential nucleation of Li plating at the edge of the electrode), the current distribution across the *in situ* electrode should be uniform. Accordingly, we have recently introduced a new *operando* platform for plan-view optical microscopy that allows for a highly uniform electric field distribution across cm-scale electrodes, and also integrates a Li metal reference electrode for 3-electrode measurement capabilities³⁴.

In this study, *operando* video microscopy was performed to directly observe Li plating and re-intercalation on graphite anodes with commercially-relevant mass loading ($>3 \text{ mAh cm}^{-2}$) under fast charge conditions (4C and 6C). The dynamic evolution of Li plating on the graphite electrode surface is correlated with the voltage profile during charging, as well as during subsequent OCV rest and discharge steps. Quantitative image analysis was performed to capture the simultaneous changes in the morphology of Li and the SoC of

graphite. *Ex situ* cross-sectional microscopy was performed to further study the re-distribution of Li-ions through the thickness of the graphite electrode, and to develop a three-dimensional understanding of changes occurring throughout the electrode volume. The voltage signatures associated with dead Li formation in the visualization cell were confirmed in pouch cells using the same electrode configurations.

The results of this study demonstrate: (1) the spatial heterogeneity of local SoC among individual graphite particles during fast charging; 2) how these spatial variations in graphite lithiation rate correlate with the nucleation of metallic Li; 3) the relationship between the Li plating/re-intercalation process and the corresponding voltage profile of the graphite working electrode; 4) dead Li formation on the graphite electrode during OCV and discharge; and 5) the re-equilibration of SoC throughout the electrode thickness during OCV rest. These findings provide a mechanistic understanding of the interactions between Li and graphite at the composite electrode level, which can be used to diagnose and mitigate Li plating during fast charging.

Visualization Approach

A three-electrode plan-view visualization cell was implemented to perform *operando* video microscopy experiments (**Fig. 1a**). The modified cell design is based on our previous reports of plan-view *operando* microscopy of Li metal anodes^{34,35}. This platform allows for imaging of electrode surfaces over large areas without current focusing due to electric field gradients³⁴. In contrast, if *operando* optical microscopy is performed with the counter electrode placed adjacent to the working electrode, large in-plane gradients in current density and SoC can develop^{8,10,34}. Compared to a cross-sectional perspective, a top-down view of the electrode provides a larger area of visual access to the working electrode (WE). This allows for visualization of the spatial heterogeneity in lithiation of graphite and Li plating across the surface. Furthermore, for all microscopy images presented in this work, 3-D focal series reconstructions are applied such that the graphite surface and the plated Li remain in focus throughout the cycling (further details in Methods section)³⁵.

To deconvolute the potential of the WE from the overpotential of the Li counter electrode (CE) and the IR drop across the electrolyte, a Li metal reference electrode (RE) is located at the side of the WE. During the experiments, galvanostatic cycling was performed between the WE and CE. The WE potential was measured and time-synchronized with the video recording from an optical microscope. The uniformity of the current distribution along the WE surface was verified by continuum scale modeling of the visualization cell (further details in the Supporting Information)^{36,37}. **Fig. 1a** shows the simulated current density distribution across the WE during 6C charging. The current density varied by less than $\pm 4\%$ across the entire electrode.

The uniform current distribution was confirmed experimentally by observing the evolution of the WE surface throughout the experiment. During slow (C/10) charging, the graphite changed color uniformly across the entire surface. The as-assembled gray electrode (**Fig. 1b**), as well as the lithiated blue (**Fig. 1c**) and gold phases (**Fig. 1d**), are shown in **Fig. 1**. During fast charging, Li plating occurred uniformly across the graphite working electrode. **Fig. 1e** shows the graphite electrode covered by a uniform layer of metallic Li after 6C charging.

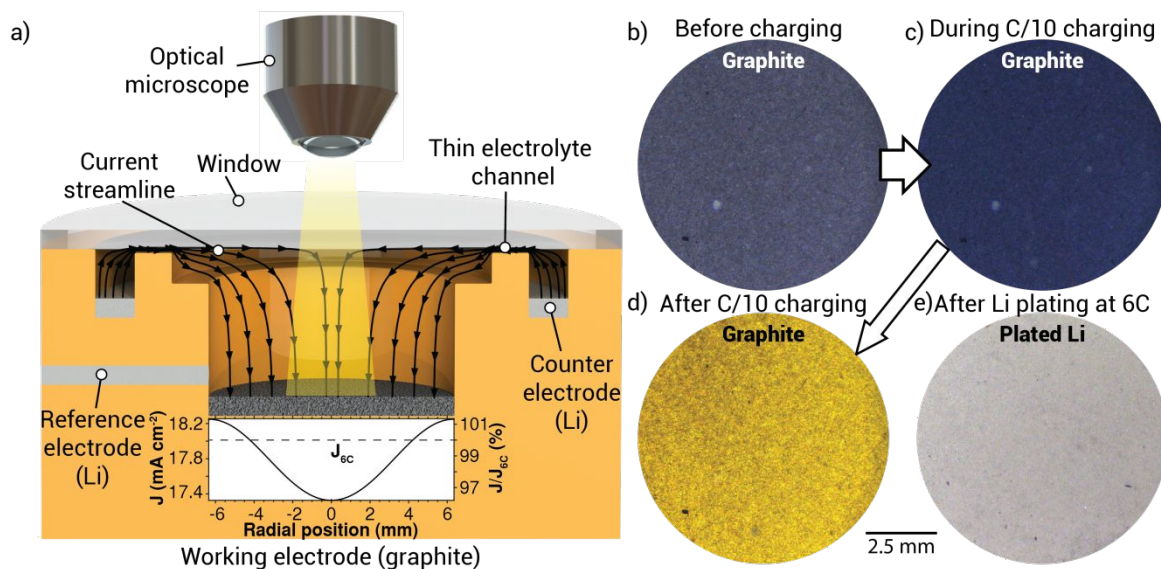


Figure 1. a) Schematic of the three-electrode *operando* visualization cell. The simulated current streamlines and the current density profile across the WE are shown (further details in Supporting Information). The streamlines visualize the direction of the current. The magnitude of the current density is shown in the Supporting Information. b-d) Images of the working electrode during C/10 charging. The homogeneous color across the electrode demonstrates the uniform current distribution of the visualization cell. e) Image of the WE after 6C charging to 85 mAh g^{-1} , starting from $E_{\text{gra}} = 0.4 \text{ V}$ vs Li/Li^+ . Li plating occurs uniformly across the electrode surface.

RESULTS

1. Color change of graphite during slow (C/10) charging

Using the visualization cell platform, C/10 charging of the graphite electrode was first performed (**Video 1** and **Fig. 2**). The voltage profile was time-synchronized with the color change of graphite (**Fig. 2a**). The color evolution of the electrode (**Fig. 2c-h**) agrees with previous reports, where the color of graphite changes from gray (unlithiated graphite) to blue (LiC_{18}), red (LiC_{12}) and gold (LiC_6) in sequence, as the SoC increases^{8,22,38,39}. X-ray diffraction (XRD) analysis was performed correlate the color of graphite with the associated lithiation stage (Fig. S1). The color difference between each lithiation stage is caused by a shift

in the plasma frequency with increasing intercalant concentration^{40,41}. A larger field of view can be found in the Supporting Information (**Fig. S2**).

The color profile can be quantified by the average RGB index across each frame. To decouple the change in color from the change in brightness, the RGB indices are normalized as described in **Eq. 3** for the example of red (further details in **Supporting Information**):

$$R\% = \frac{R}{R + G + B} \#(Eq.3)$$

where R , G and B are the average R, G and B index of a frame, respectively, and $R\%$ is the normalized R .

Fig. 2b shows the three normalized color curves as a function of specific capacity and SoC.

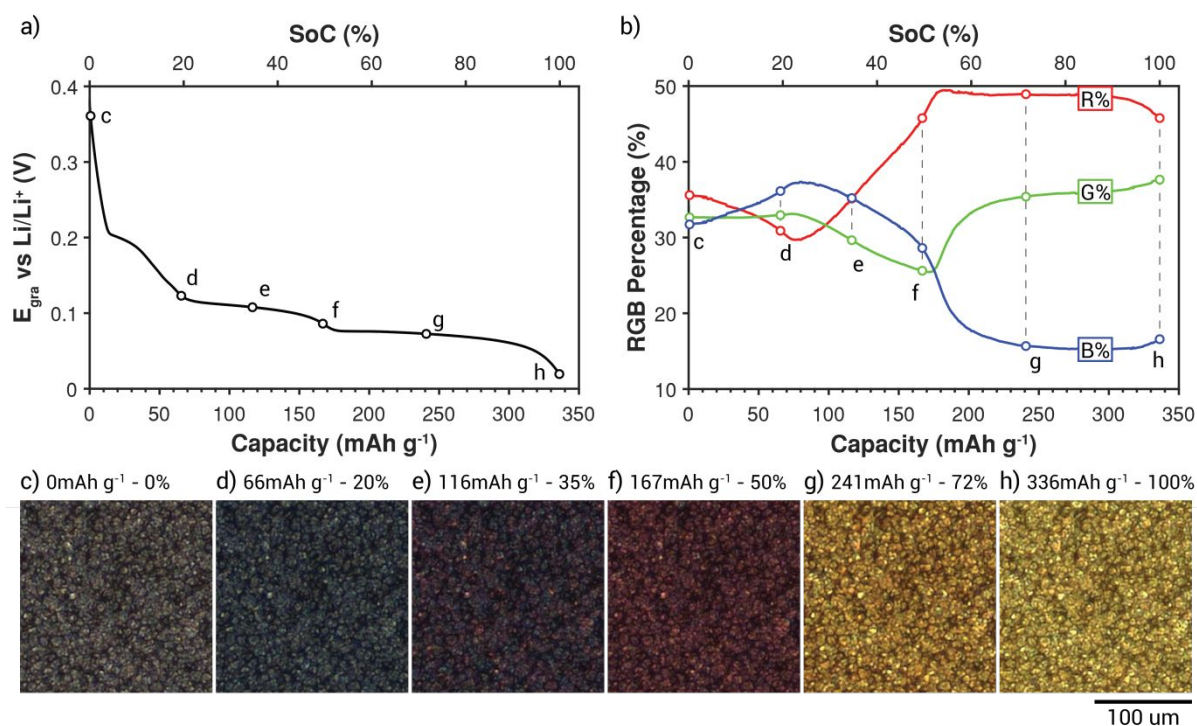


Figure 2 a) Voltage profile of the graphite WE. 100% SoC is defined as the capacity at which the C/10 discharge voltage reaches $V = 20 \text{ mV}$. **b)** The normalized RGB indices of the field of view during C/10 lithiation. **c) – h)** Operando color evolution of the WE during C/10 lithiation. The color of graphite transitions from gray to blue, red, and gold as the SoC of graphite increases.

2. *Operando* visualization of Li plating during 6C charging

As shown in **Video 2** and **Fig. 3**, *Operando* video microscopy was performed on a graphite WE during 6C galvanostatic charging. Individual graphite particles (with an average diameter of 8 μ m) can be clearly resolved in these *operando* images. The WE potential was 0.4 V vs Li/Li⁺ before charging (**Fig. 3a, b**). Constant current (CC) charging was performed until a specific charge of 85 mAh g⁻¹. Throughout this paper, specific charge is calculated using the mass of graphite in the electrode. It can be noted that the potential of the graphite WE dropped below 0V vs. the Li/Li⁺ RE at a time of $t = 8.5$ s (4.3 mAh g⁻¹) after the initiation of charging. Furthermore, the potential continued to drop until $t = 104$ s (52 mAh g⁻¹) as the color of the graphite evolved from gray to blue and then to gold (**Fig. 3b-e**).

Unlike the homogeneous C/10 lithiation shown in **Fig. 2**, spatial heterogeneity was observed across the graphite surface during 6C charging. In **Fig. 3d**, after 63 s (32 mAh g⁻¹), distinct blue (LiC₁₈), red (LiC₁₂) and gold (LiC₆) regions can all be observed on the electrode surface. This demonstrates that individual particles lithiate at different rates, which could be caused by differences in crystallographic orientation, morphology, interfacial resistance, and size⁴²⁻⁴⁴. As will be described below, the in-plane spatial heterogeneity of charging rates between particles impacts the subsequent nucleation of Li metal plating.

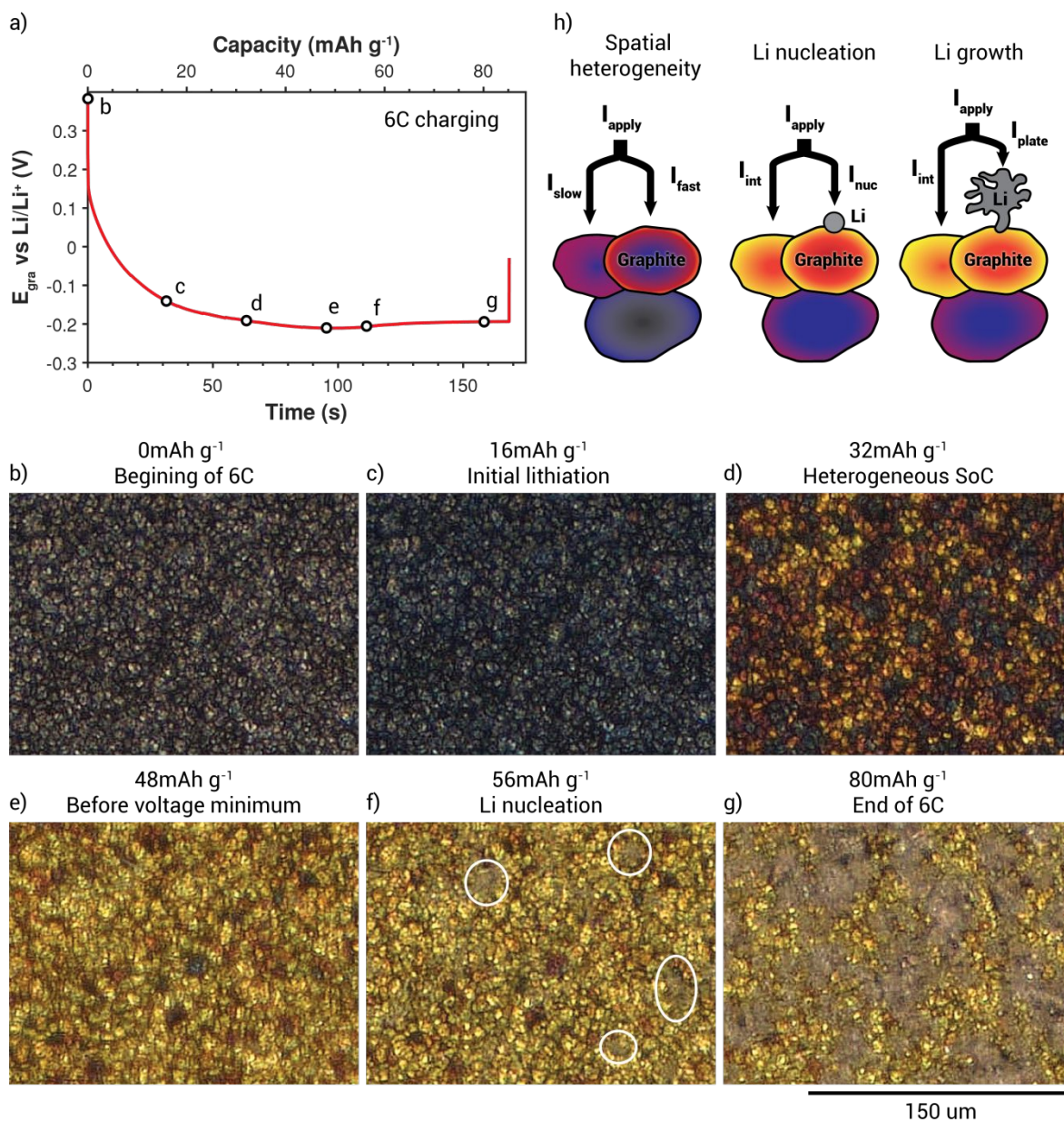


Figure 3 a) Voltage profile of the graphite WE during 6C charging; **b) – g)** Still frames of the WE during 6C charging. Plated Li is circled in f). The time and the voltage of graphite at each frame is labeled in a); **h)** Schematics showing the current pathways for lithiation and Li plating during fast charging.

The anode potential (vs. the Li/Li⁺ reference) reached a minimum at 104s (52 mAh g⁻¹), and Li nucleation was observed in the first frame after this voltage minimum (**Fig. 3f**). The voltage minimum during fast charging has been attributed to the onset of Li plating^{17,21}. As a visual aid, various plated Li deposits are highlighted with circles in **Fig. 3f**. The individual Li deposits continue to grow during the remainder of the 6C charge (**Fig. 3g**). The Li plating process can be more clearly observed in **Video 2**. The evolution of the mossy Li morphology observed is consistent with our previous studies of Li metal anodes^{34,45}. The process of Li plating on graphite during fast charging is summarized in **Fig. 3h**. Over a larger field of view, the heterogeneous nature of graphite lithiation can be observed across the electrode surface, and the nucleation density of Li along the surface is consistent with **Fig. 3** (Supporting Information **Fig. S3**).

The plated Li was observed to preferentially nucleate on the particles that exhibited the fastest increase in surface Li⁺ concentration. **Fig. 4** provides a comparison of the same location on the electrode surface after 63 s (32 mAh g⁻¹) and after 126 s (64 mAh g⁻¹) of charging. Similar to **Fig. 3d**, in **Fig. 4a** we observe that after 63 s (32 mAh g⁻¹) charging, some of the particles turned gold, while others exhibited the red or blue phases. The dotted white curves outline the location of plated Li after 126 s (64 mAh g⁻¹, **Fig. 4b**). The nucleation locations for Li deposits correlate well with the particles that turned gold first during fast charging. We note that while not all of the gold areas in **Fig. 4a** are covered by plated Li after 126 s-64 mAh/g charging, there is a clear statistical preference for nucleation at these “hot spots”.

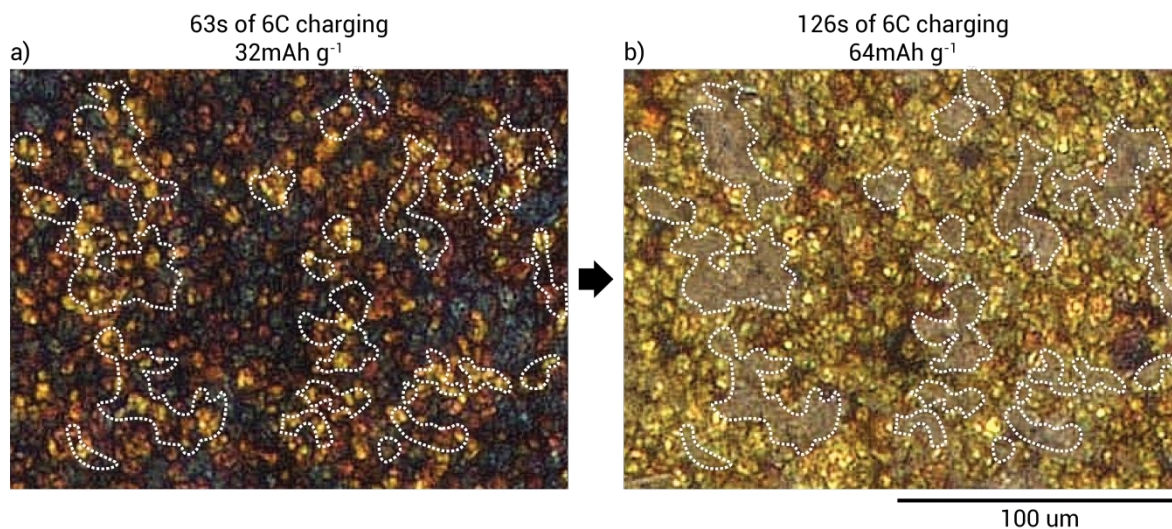


Figure 4 a) Graphite electrode after 63 s (32 mAh g^{-1}) charging at 6C; and **b)** The same area of electrode after 126 s (64 mAh g^{-1}) charging at 6C. To provide a visual aid, plated Li is manually labeled with white dashed lines in b). The dashed lines are shown in the same locations in a) to show that some of the particles that turned gold first served as nucleation sites for Li plating.

The heterogenous SoC distribution during charging results from variations in the local rate of lithiation among the particles (**Fig. 3h**). Previous studies have shown that particles with graphene planes oriented along the normal vector to the surface lithiate faster^{43,44}. A low solid-state diffusivity and larger particle size can also lead to surface saturation before the particle is fully filled with Li^+ ¹⁷. These variables will impact the flux balance between rate of insertion (surface kinetics) and the rate of solid-state diffusion away from the surface within individual particles, which will determine the surface concentration of Li^+ as a function of time.

The rate of lithiation for individual particles may vary with time throughout the charging process, where particles that initially lithiate fastest slow down as their surface concentration approaches saturation. This can cause a transition in reaction pathways wherein the constant flux of Li^+ ions provided to the anode surface is either re-directed to other particles that have not yet reached a saturation in surface concentration, or lithium plating initiates (**Fig. 3h**). Under galvanostatic conditions, the total current associated with these

reaction pathways must sum to the applied current. The fractional distribution of current between these reaction pathways will be determined by the time-variant impedance of each pathway, analogous to the nucleation and growth behavior in Li metal anodes⁴⁵. Before the onset of Li plating, the applied current (I_{app}) is associated with the intercalation of Li^+ into graphite. After Li plating occurs, new current pathways for Li nucleation (I_{nuc}) and growth (I_{plate}) are developed, and thus the current for Li^+ intercalation into graphite (I_{int}) is less than the total applied current (I_{app}). As a result of irreversible Li plating, the average Li content in the graphite was measured to be lower after fast charging than after slow charging using XRD (**Fig. S4**).

As the experimental results in **Fig. 3** demonstrate, the particles associated with the lowest initial impedance for lithiation (those that turn gold first) are also associated with the lowest impedance for nucleation. Therefore, Li plating nucleates on these particles, even after adjacent particles have experienced an increase in their surface Li^+ concentration. Evidence for this behavior can be seen in the transition from **Fig. 3e** to **Fig. 3f**, where most of the particles have transitioned to a gold color, but nucleation of Li plating occurs on the subset of particles that turned gold first (**Fig. 4a**). We note that because of the relatively wide SoC window associated with the gold color (**Fig. 2b**), adjacent particles with a similar gold color can still be at a different SoC. In the future, modeling efforts to decouple these individual reaction pathways will be valuable to elucidate the mechanistic origins of the observed differences in reaction rates.

3. *Operando* visualization of OCV rest after Li plating

After charging, the graphite electrode shown in **Fig. 3** was subsequently held at OCV for 1 hour. The OCV rest and the following C/5 discharge periods are shown in **Fig. 5** and **Video 3**. During the first 69s of OCV rest, the plated Li shrank in size (**Fig. 5b-c**). A portion of the Li deposits also changed color from a metallic gray luster to black. These morphological changes can be more clearly visualized in **Video 3**. We have previously reported similar darkening of electroplated Li when stripping from mossy dendrites deposited

on Li metal anodes^{34,45,46}. Specifically, as Li⁺ ions are stripped from the plated Li, the associated volumetric contraction results in mechanical detachment (and/or electrical isolation) of the remaining metallic Li, which is encapsulated in an insulating SEI layer. This surface SEI layer on the remaining dead Li experiences roughening as the volume decreases, reducing the reflectance of the surface (**Fig. S5** in the Supporting Information). As discussed below, the volumetric contraction provides evidence for the re-intercalation of the plated Li into graphite during the OCV hold, which is consistent with previous studies using NMR and EPR^{7,14,20}.

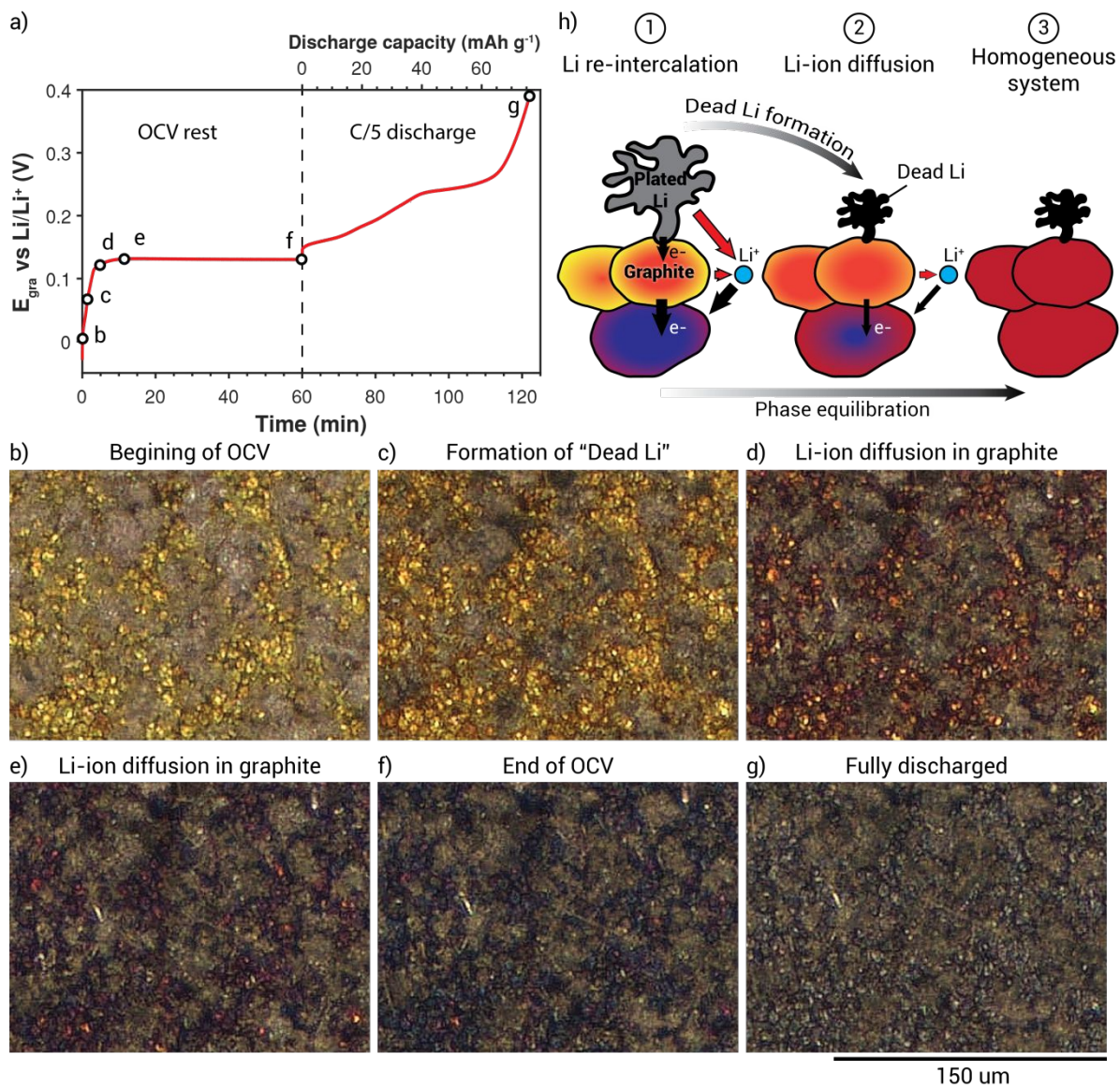


Figure 5 a) Voltage profile of the graphite WE during OCV rest and C/5 discharge; **b-g)** Still frames of the WE during OCV rest and C/5 discharge until 0.4 V vs. Li/Li^+ . The time for each frame is shown in panel a; **h)** Schematics showing the ionic and electronic pathways for Li re-intercalation and "dead Li" formation during OCV rest.

Although it is known that metallic Li reacts with the electrolyte to form an SEI layer on the plated Li surface⁴⁷, these electrolyte decomposition reactions alone will not cause the observed shrinkage of Li. To deconvolute the effects of SEI formation from Li re-intercalation, visualization experiments were performed on another electrode that was subjected to overcharge conditions. This electrode was fully lithiated to 20 mV vs Li/Li⁺ at C/10 (349 mAh g⁻¹) before being charged at 6C for an overcharge of 26.6 mAh g⁻¹. Under these conditions, there is no pathway for Li re-intercalation into the fully lithiated graphite.

As shown in **Fig. S6** (Supporting Information), during the 8 min OCV rest after overlithiation, no observable volume reduction or color change of the plated Li occurred. After the OCV rest, a C/5 discharge current was applied, and concurrent dead Li formation was observed. These results demonstrate that SEI formation alone, which occurs during the 8 min OCV rest after overlithiation, does not cause the decrease in volume or change in color observed in **Fig. 5b-c**; instead, the volumetric contraction and associated dead Li formation primarily results from the re-intercalation of plated Li into graphite.

For the electrode that was not overcharged (**Fig. 5**), the re-intercalation process (and associated dead Li formation) during the OCV step occurred as the voltage increased between points b and c in **Fig. 5a**. The morphology of the remaining Li did not change significantly throughout the remainder of the 1 hr OCV rest or the subsequent C/5 discharge (**Fig. 5d-g**). This shows that the remaining inactive Li on the surface was dead Li that was electrically and/or electrochemically isolated.

The color of the graphite surface changed during OCV rest, reflecting a local decrease in the SoC of the graphite particles on the surface. At the beginning of the OCV rest, the graphite surface exhibited the golden color associated with LiC₆ (**Fig. 5b**). During the formation of dead Li, the color of graphite changed to orange, which illustrates that the LiC₆ transitioned towards the LiC₁₂ phase as the SoC equilibrates within individual particles and throughout the thickness of the electrode (**Fig. 5c**).

As we will demonstrate in Section 4, the re-intercalation of plated Li and the reduction in SoC of the graphite at the surface are mainly driven by galvanic corrosion processes. The schematic in **Fig. 5h** illustrates the concurrent Li-ion and electron fluxes in the system. At the beginning of the OCV rest, the plated Li is electrically connected to the graphite electrode. The gold graphite particles at the electrode top surface are at higher SoC, while particles near the current collector are at lower SoC, which is primarily attributed to mass transport limitations during fast charge³⁶. During the OCV rest, oxidation occurs at both the plated Li and the graphite particles at the top of the electrode. At the same time, reduction occurs at the graphite particles at lower SoC. In addition, Li⁺ concentration gradients can also relax within the electrolyte, which will affect the local electrolyte potential as a function of depth within the electrode. Electrons pass through the plated Li and graphite particles to maintain charge neutrality. These observations are consistent with the predictions of a previous modeling study of Li re-intercalation into graphite after fast charging⁴⁸. In Section 4, *ex situ* cross-sectional imaging will be presented to provide further evidence of this galvanic corrosion mechanism.

The graphite surface continued to change in color after the formation of dead Li. The majority of the graphite particles evolved in color from orange to red (LiC₁₂), and then to blue (LiC₁₈) at the end of the OCV rest (**Fig. 5d-f**). These phase transitions are attributed to re-equilibration of the electrochemical potential throughout the thickness of the graphite electrode (**Fig. 5h**). During the subsequent C/5 discharge, the graphite color continued to evolve. The particles eventually returned to the initial gray color of graphite at the end of the discharge step (**Fig. 5g**). A larger field of view for the OCV rest and the subsequent discharge step can be found in **Fig. S7** in the Supporting Information.

One variable that will influence the extent of Li plating and subsequent re-intercalation is the amount of charge passed during fast charging. Therefore, to study the influence of depth of charge on the dynamic evolution of the plated Li/graphite system, an additional visualization experiment was performed. Similar to cell A (which was described in **Fig. 3-5**), the new cell (cell B) was also fast charged at 6C and then rested at OCV. However, the total charge capacity was 85 mAh g⁻¹ in cell A, while the charge capacity of cell B

was 121 mAh g⁻¹. Detailed *operando* imaging of cell B is provided in Supporting Information **Fig. S8**. Because these cells were both fast charged at the same 6C rate, the initiation of Li plating occurred at approximately the same time (105 s in A and 90 s in B). Therefore, cell B experienced significantly more Li plating at the end of the charge step, since Li metal continued to plate for a longer duration in cell B.

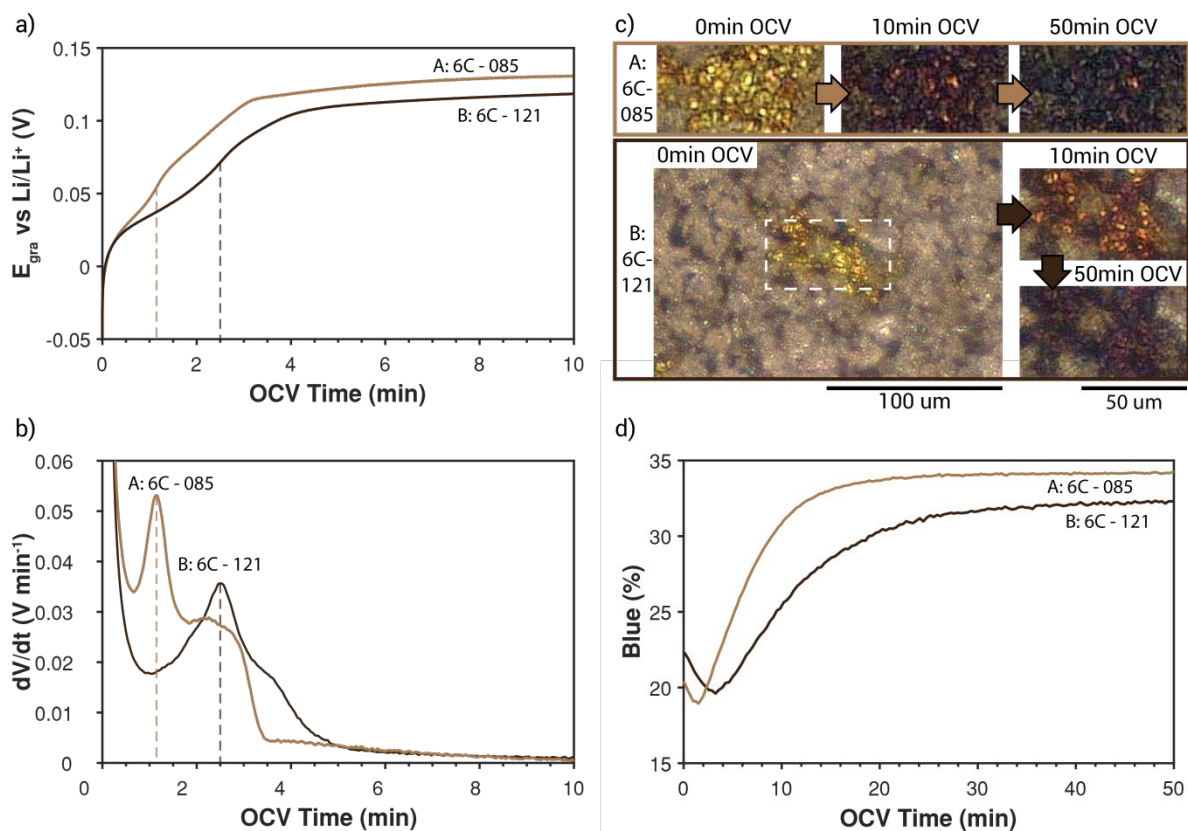


Figure 6 **a)** Voltage profiles of graphite during a 10 min OCV rest period for two cells that were charged with the following conditions: after 6C charging until a capacity of 85 mAh g⁻¹ (cell A) and after 6C charging until a capacity of 121 mAh g⁻¹ (cell B); **b)** dV/dt curves associated with the two voltage profiles. The peaks are labeled with dashed lines in panels **a** and **b**; **c)** local optical images of the graphite surfaces at different points in time during the OCV rest; **d)** Blue% of graphite during the extended 50 min OCV rest period.

Fig. 6a shows the voltage traces of the two graphite WEs during the first 10min of the OCV rest. For both cells, Li shrinkage was observed via *operando* microscopy during the initial rise of the electrode potential. As dead Li formed, a deflection in the voltage profile was observed. To further quantify this electrochemical signature, differential voltage analysis was performed (**Fig. 6b**)^{30,32}. The local maxima, which can be observed as peaks in the differential voltage plot, correlate to the points with the steepest slopes in the voltage profile. The dV/dt peaks of the two cells occurred at 69 s and 150 s of OCV rest, respectively. The locations of the maxima are labeled by dashed lines in **Fig. 6a-b**. In contrast, during the OCV rest after C/10 charging (where no Li plating occurred), a deflection was not observed in the voltage profile, and no peak was observed in the dV/dt profile (**Fig. S9**).

For both cells, the majority of the plated Li stopped changing in morphology before the electrode voltage reached steady-state (**Fig. 5, S7-8**). This demonstrates that dead Li formation occurs during the time period when the voltage is rising, which can be highlighted in the differential voltage curve (**Fig. 6a-b**). The dV/dt peak occurs later in the OCV profile for cell B, which indicates that the time required for re-intercalation increases as a result of the larger volume of Li plated (**Fig. 6c**). This is also consistent with the *operando* microscopy results, where dead Li formation occurred after a longer period of time in cell B (**Video 4**). Comparing the surface coverage of dead Li between the two cells at the end of the OCV rest (**Fig. S8h** and **Fig. 5g**), a larger amount of dead Li is present in cell B, indicating that the volume of residual dead Li increases as the volume of plated Li increases. The correlation between the amount of the plated Li and the resulting amount of dead Li has also been observed in *operando* video microscopy of Li metal anodes³⁴.

During the 50 min period of OCV rest, a portion of the graphite surface was not covered by plated Li and remained visible (**Fig. 6c**). This allowed for the local variations in the color of the graphite surface to be tracked in these exposed regions. At the beginning of the OCV rest periods, the surfaces of graphite were gold for both cells. Although for both cells, the dead Li was fully formed within the first 4 min of OCV rest, the color of graphite did not reach equilibrium until an extended rest period. After 10 min of OCV rest, the graphite area for cell A changed in color to red, and the graphite area for cell B changed in color to

orange/gold. This indicates that the local SoC of the surface decreased for both cells, but remained higher in cell B. The local SoC of the surface continued to decrease in both cells before reaching a stable color profile after 20-30 min OCV rest. After 50 min of OCV rest, the exposed graphite area for cell A was mostly blue (associated with the LiC_{18} phase), while cell B was a mixture of blue and red (associated with the LiC_{12} phase). For both cells, the morphology of the plated Li did not change throughout the C/5 discharge, confirming that all of the remaining Li on the electrode surface was dead Li (**Fig. 5g, S5-6**).

The difference in color at the end of the OCV rest between cell A and cell B indicates that the equilibrium SoC of graphite was larger in cell B than in cell A. This was further confirmed by the fact that the subsequent discharge capacity was larger in cell B (**Fig. S7-8**). The discharge capacity of cell A was 76 mAh g^{-1} and the discharge capacity for cell B was 97 mAh g^{-1} . However, the difference in discharge capacity (21 mAh g^{-1}) was less than the difference in charge capacity (36 mAh g^{-1}) between the cells, indicating that a larger loss in Li inventory occurred for the cell that was fast charged for a longer time. This is also consistent with the observation of a larger volume of residual dead Li in cell B than cell A, indicating that Dead Li formation is a significant contribution to Coulombic inefficiency during fast charging.

4. Cross-sectional visualization of OCV rest after Li plating

To study the through-plane re-equilibration of Li^+ into the depth of the graphite electrode during OCV rest, *ex situ* cross-sectional imaging was performed on five Li metal-graphite coin cells. Before the OCV rests, the five cells were all galvanostatically charged at 6C until a charge capacity of 200 mAh g^{-1} . The cells were then subjected to OCV rest periods of 0 min (**Fig 7.b**), 9 min (**Fig 7.c**), 12 min (**Fig 7.d**), 24 min (**Fig 7.e**) and 36 min (**Fig 7.f**), respectively. After the OCV rests, the cells were immediately disassembled in an Ar glovebox, and the electrodes were rinsed with dimethyl carbonate (DMC) to remove excess electrolyte. Further details on the disassembly process are provided in the Method section. Cross-sectional optical microscopy images were captured to study the impact of OCV rest time on the through-plane SoC gradient.

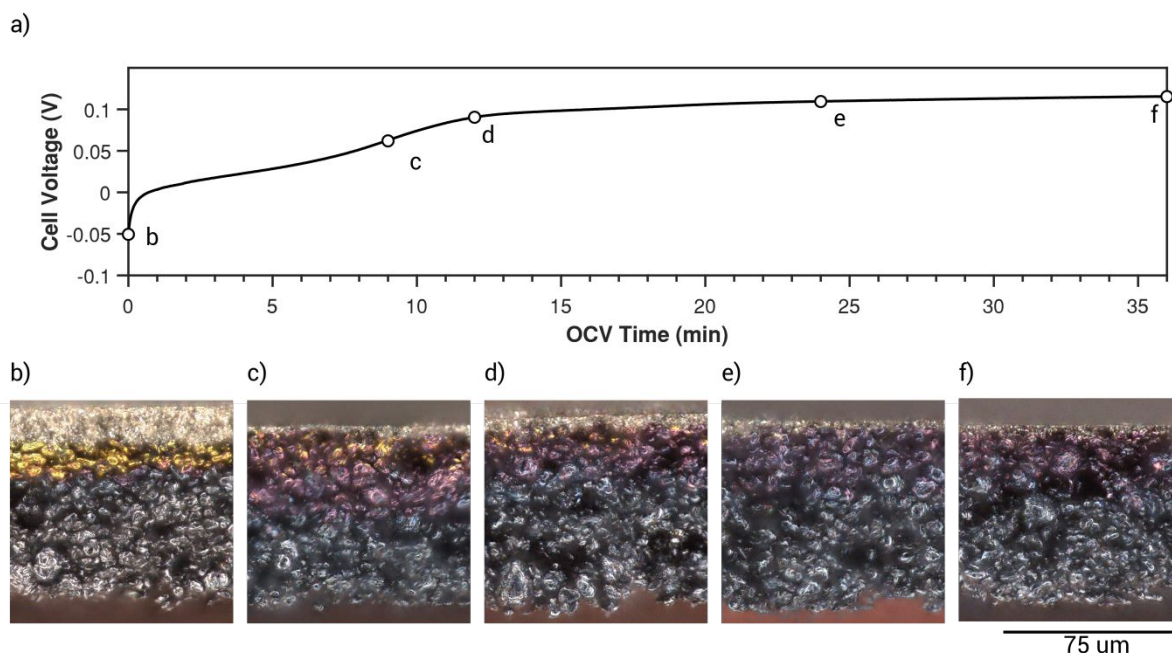


Figure 7 a) Voltage profile of the Li-graphite coin cell during a 50min OCV rest period; and **b-f)** postmortem cross-sectional images of 5 coin cells after different durations of OCV rest, as indicated in the voltage profile in panel **a**.

Similar to the *operando* cells, the voltage profiles of the coin cells exhibited distinct voltage features that correspond to the re-intercalation of plated Li (**Fig. 6a and 7a**). The voltage increased during the OCV rest and a deflection was observed before the voltage reached equilibrium.

For the electrode that was disassembled immediately after 6C charging, plated Li was only observed at the top surface (**Fig. 7b**). Owing to the stack pressure of the coin cell, the plated Li is more compact than the mossy structures observed in the visualization cell, which arises from viscoplastic deformation of Li metal against the polymer separator during plating⁴⁹. Traversing from the top surface of the electrode to the bottom surface, a gradient can be observed in the color of the electrode from gold (LiC_6) to red (LiC_{12}), blue (LiC_{18}), and then gray (C). The observation of the LiC_6 phase toward the top of the electrode indicates that the local SoC near the top is significantly higher than the total charge capacity of 200 mAh g^{-1} . This

indicates that the local C rate near the top surface was much higher than 6C, which is attributed to current focusing effects^{36,37}. These results are also consistent with our plan-view *operando* observations that the top surface of the graphite electrode was gold (LiC_6) when Li plating occurred (**Fig. 3f**). The variation in local SoC throughout the thickness of the electrode has also been observed in *operando* synchrotron XRD experiments¹⁶. The gradients in SoC within the thick graphite electrodes used in this study arise from coupled thermodynamic, mass transport, and kinetic phenomena during fast charging^{36,37}.

After 9 min of OCV rest, the thickness of the Li layer reduced from 15.2 μm (**Fig. 7b**) to 4.1 μm (**Fig. 7c**). This is caused by the re-intercalation of plated Li during OCV rest, as shown in the *operando* results above (**Fig. 5-6**). The thickness of the plated Li did not change significantly between the four cells with 9 min to 36 min OCV rests (**Fig. 7c-f**), indicating that only dead Li remained on the surface after 9 min of OCV rest. The voltage deflection occurred prior to disassembling the cell in **Fig. 7d**. This is consistent with the observation in the *operando* cell, where dead Li formation was associated with voltage deflection.

Besides the reduction in the thickness of the Li layer, color change of graphite also occurred in the first 9 min of OCV rest. The particles near the top surface of the electrode changed color from gold (LiC_6) to red (LiC_{12}). The phase boundary between blue (LiC_{18}) and gray (C) particles also propagated towards the bottom of the electrode. These observations demonstrate that Li ions from the plated Li and the high SoC graphite particles at the top of the electrode equilibrate with the low SoC graphite particles near the bottom during the OCV rest period.

During 12-36min of OCV rest, as the graphite particles are going through the re-equilibration process, the particles near the top surface continued to decrease in SoC (**Fig. 7d-f**). Because of this decrease, during the period from 9 min to 12 min of the OCV rest, the phase boundary between the red (LiC_{12}) and blue (LiC_{18}) particles propagated towards the top of the electrode.

Combining the plan-view and cross-sectional observations, the Li re-intercalation and the graphite SoC re-equilibration during OCV rest can be rationalized, as was described schematically in **Fig. 5h**. Immediately

after fast charging, because of current focusing towards the top of the electrode, graphite particles at the electrode-separator interface are at a higher local SoC than within the electrode bulk^{36,37}. The graphite particles and the plated Li are all in electrical contact. Owing to the differences in the local electrochemical potential among the graphite particles at different phases, as well as between graphite and Li, there exists a driving force for galvanic corrosion currents throughout the electrode. At the same time, diffusion of the Li⁺ in the electrolyte relaxes the concentration gradients that had formed in the electrolyte.

Local oxidation and subsequent Li-ion dissolution into the electrolyte occur at the surface of both the plated Li and graphite particles with higher SoCs, which results in stripping of metallic Li and a decrease in the local SoC of graphite⁴⁸. A concurrent reduction reaction must also occur, which manifests as Li-ion intercalation into graphite particles deeper within the electrode bulk that are initially at a lower SoC. Electrons are transported via conduction through the solid-solid contact points within the electrode, which maintains charge neutrality of the system.

Solid-state diffusion of Li-ions through the depth of the electrode could also occur, but at room temperature and atmospheric pressure, the rate of such processes are much slower than the galvanic corrosion process^{40,50}. To prove that solid state diffusion alone cannot cause the re-equilibration phenomena observed in **Fig. 7**, a coin cell was disassembled and rinsed immediately after fast charging. Cross sectional images were captured 20 min after disassembly and 110min after disassembly (**Fig. S10**). No significant color change of graphite or volume reduction of Li was observed, proving that the galvanic corrosion current is the main driving force for Li re-intercalation and graphite SoC re-equilibration during OCV rest.

These observations are consistent with the process schematic shown in **Fig. 5h**. During the re-intercalation of plated Li, volumetric contraction caused portions of the metallic Li to become disconnected (and/or kinetically restricted) from the graphite, forming dead Li. Although the dead Li was no longer active in the electrochemical reaction, a driving force still existed for re-equilibration of graphite particles at different local SoC. Therefore, after dead Li formation, the SoC of particles near the electrode-separator interface continued to decrease, while the SoC for the particles in the bulk electrode continued to increase. After

extended OCV rest, the system approached equilibrium as most of the graphite particles reached the same potential.

5. *Operando* visualization of discharge after Li plating

To study the impact of immediate discharge on Li re-intercalation, another *operando* experiment was performed (**Fig. 8**). Cell C followed the same charging protocol as cell A (**Fig. 3-5**) where it was charged at 6C until a capacity of 85 mAh g⁻¹, but then cell C was immediately discharged at a C/5 rate without an OCV rest period.

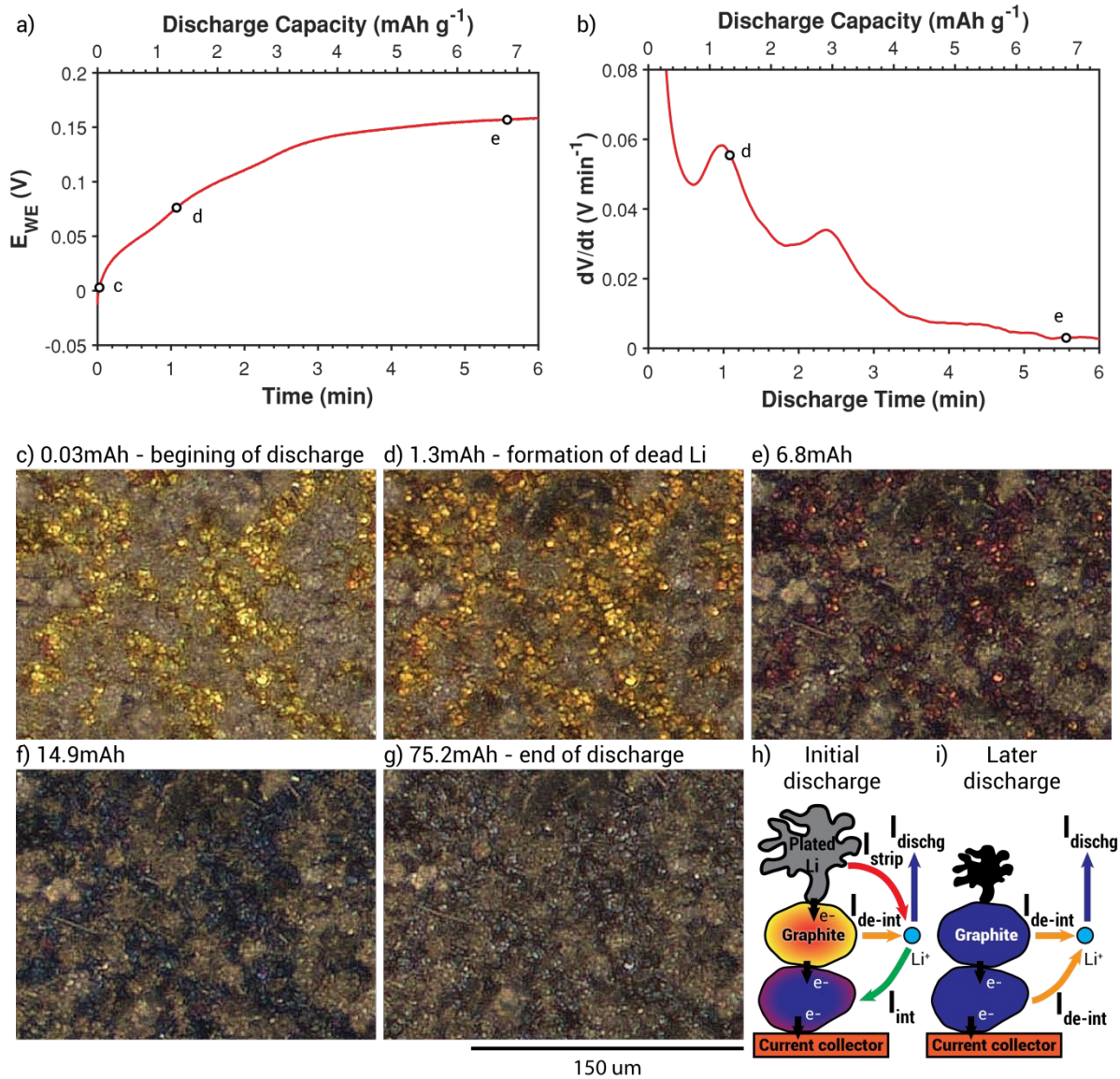


Figure 8 a) Voltage profile of graphite during C/5 discharge after 6C charging until a capacity of 85 mAh g^{-1} ; **b)** dV/dt curve of the voltage profile; **c-g)** Still frames of the WE during discharge until 0.4 V vs. Li/Li^+ . The time for frame c-e is shown in panel a and b; **h)** Schematics showing the ionic and electronic pathways for Li re-intercalation and graphite SoC re-equilibration during discharge.

The voltage profile during the first 10 min of the C/5 discharge of cell C is shown in **Fig. 8a**. Similar to the cells that were rested at OCV (**Fig. 5-6**), dead Li formed during the voltage deflection at the beginning of discharge (**Fig. 8 c-d**). This voltage deflection corresponds to the initial peak in the dV/dt profile (**Fig. 8b**).

The morphology of the dead Li remained unchanged throughout the subsequent discharge. The color of the graphite evolved from gold (LiC_6) to red (LiC_{12}) and blue (LiC_{18}), and it finally turned gray (C) at the end of discharge (**Fig. 8d-g**). The extended voltage profile of cell C throughout the entire discharge process can be found in the Supporting Information (**Fig. S11**).

The second peak in the dV/dt plot is therefore attributed to the phase transitions of graphite during discharge. In addition to the re-intercalation of plated Li, transitions between the graphite stages can also lead to deflections in the voltage profile⁵¹. Double peaks in the dV/dt plot following fast charging have also been observed in a previous study⁵², and will depend on the SoC distribution in graphite after fast charging and the C-rate of discharge.

The concurrent reaction pathways that occur during discharge are shown schematically in **Fig. 8h**. The total discharge current determines the required flux of Li ions from the WE to the counter electrode (corresponding to current denoted by I_{dischg}), which must be supplied by the net sum of the corresponding oxidation reactions from the WE. Immediately upon discharge, this flux can be supplied by both the Li metal (corresponding to I_{strip}) and the graphite particles with a high local SoC (corresponding to $I_{\text{de-int}}$). Concurrently, there is a driving force for re-equilibration of the SoC of graphite, which is driven by the SoC gradient that formed during fast charging, and will also be affected by concentration gradients in the electrolyte. This results in an intercalation current at the graphite particles in the bulk of the electrode (I_{int}). In order to conserve charge, the total oxidation and reduction currents must balance according to the following equation:

$$I_{\text{dischg}} + I_{\text{int}} = I_{\text{strip}} + I_{\text{de-int}} \quad (4)$$

The distribution of fluxes throughout the electrode volume has been described in previous modeling studies⁴⁸. Later in the discharge step, only dead Li remains on the surface, and therefore I_{dischg} must be supplied completely by $I_{\text{de-int}}$ until the graphite has been fully discharged (**Fig. 8i**).

6. Li plating in pouch cells

In order to study the voltage signature of Li re-intercalation in conventional cell formats, pouch cells were fabricated. Three graphite-NMC pouch cells were charged using a constant current-constant voltage (CC-CV) protocol at a 6C rate until 4.2 V, with a C/10 cutoff current during the CV step. After the charging half cycle, the cells were then rested at OCV for 0min, 5 min and 30 min, respectively. After the OCV period, they were discharged at a C/2 rate until 3 V.

Fig. 9a shows the voltage profiles of the cells during the first 20min after the charging step. Similar to the *operando* cells, deflections in the voltage profile were observed for the three cells, which occurred during OCV or during discharge, depending on the length of the rest period. The deflection feature is further identified by the peak in the dV/dt profiles (**Fig. 9b**). As observed in the *operando* cells and the coin cells, this voltage feature is related to dead Li formation, which was confirmed with post-mortem optical imaging of the three cells (**Fig. S13** in the Supporting Information).

To verify that the voltage plateau and the peak in the dV/dt curve is associated with Li plating, another NMC-graphite pouch cell was charged at a C/2 rate before undergoing OCV rests and discharge (**Fig. S12** in the Supporting Information). No Li re-intercalation signatures were observed during the OCV or discharge steps.

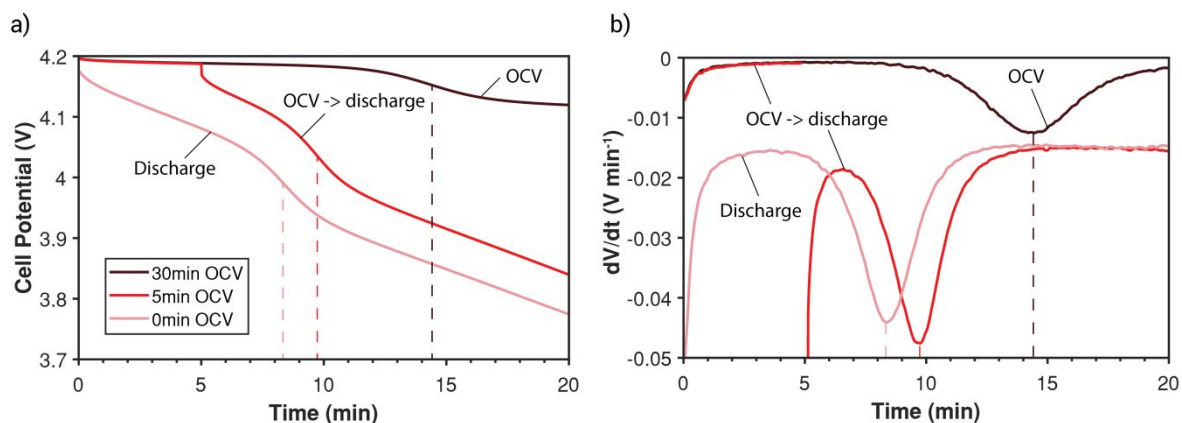


Figure 9 a) Voltage profiles of three pouch cells during the first 10min of OCV/discharge after 6C charging; **b)** dV/dt analysis shows a peak that is similar to what is observed in the visualization cells and coin cells. The local minima in the dV/dt profiles are labeled with dashed lines in panel a and b.

After fast charging, the application of a discharge current reduces the time required to fully form dead Li. The peaks of the dV/dt curves occurred at different times, namely, 8.3 min, 9.7 min, and 14.4 min after charging for the cell with 0 min, 5 min and 30 min OCV rest periods, respectively. However, despite the differences in the time required for dead Li formation, the three cells had very similar discharge capacity and Coulombic efficiency (**Table S1 in the Supporting Information**). The consistency in these values suggest that the extent of Li inventory loss from dead Li and SEI formation in the three cells is not strongly influenced by the OCV rest time. It also highlights that when comparing experiments with different discharge protocols, the relative amount of charge passed before the dV/dt peak (which differs among these cells) should not be used as a proxy for the amount of dead Li formed.

CONCLUSION

In this work, three-electrode *operando* video microscopy was performed on calendared graphite electrodes to gain insights into the dynamic evolution of Li plating and re-intercalation under fast charging conditions. Specifically, several key understandings were developed:

(1) Individual graphite particles within the electrode lithiate at different rates, and the relative rate of lithiation influences the location of Li metal nucleation

During fast charging, spatial heterogeneity in the local SoC of individual graphite particles was observed. In particular, the rate of lithiation varied among particles. The particles that exhibited the gold color associated with the LiC_6 phase fastest served as the nucleation sites for Li plating.

(2) The onset of Li plating correlates with the local minimum of the graphite electrode potential.

A three-electrode configuration within the *operando* microscopy cell was employed to decouple the graphite WE potential from the full cell potential. Analogous to nucleation behavior in Li metal anodes, the potential of the graphite WE first dropped below 0V vs. Li/Li^+ , and the onset of plating was first observed after the graphite potential passed through a local minimum during fast charging.

(3) Galvanic corrosion currents are the main driving force for dead Li formation, Li re-intercalation, and graphite SoC re-equilibration

Immediately after fast-charging, the size of plated Li deposits decreased until dead Li formed. This process is associated with Li re-intercalation, which does not occur under over-charging conditions. Therefore, the driving force for re-intercalation is a galvanic corrosion reaction, which is driven by the difference in electrochemical potential between plated Li and graphite. Post-mortem cross-sectional analysis showed that local SoC gradients throughout the electrode thickness relax during OCV when in contact with the electrolyte, but the local SoC gradients are retained if the electrode is removed from the electrolyte. This demonstrates that galvanic corrosion reactions between graphite particles are responsible for the re-equilibration in SoC throughout the electrode thickness.

(4) Electrochemical signatures during OCV rest or discharge are associated with dead Li formation

After fast charging, *operando* analysis was performed with either an OCV rest or an immediate discharge step. In all cases, a deflection in the voltage curve was observed, which correlated in time with the formation of Dead Li. Finally, the Coulombic efficiency of pouch cells was compared to the associated voltage profiles during fast charging. The results suggest that although the application of a discharge current reduces the time required for dead Li formation, the reversibility of plated Li is not strongly influenced by the rate of dead Li formation.

(6) Future impact

This work provides new insight into Li plating dynamics during on graphite during fast charging, as well as the interactions between the plated Li and graphite during OCV rest and discharge steps. The fundamental understanding in this work can be leveraged to inform novel strategies for battery material design for fast-charge applications. For example, the heterogeneity in local SoC among different graphite particles will be influenced by differences in solid-state diffusivity, size, and surface kinetics. Therefore, strategies to minimize variations in these properties among different particles within the electrode will suppress local current focusing, and thus reduce the driving force for Li nucleation. Additionally, because Li nucleation occurs at the local minimum of graphite potential (below 0 V vs. Li/Li⁺), strategies to adjust the nucleation overpotential or control the charging protocol in a careful manner could allow for fast charging with the anode at potentials below 0 V. Finally, as shown here, galvanic corrosion currents dictate dead Li formation, re-intercalation dynamics, and re-equilibration of local SoC throughout the graphite thickness. Therefore, strategies to modify this corrosion behavior (such as advanced electrolyte design) could be leveraged to control the dynamics and relative fluxes of different reaction pathways along the electrode surface in a manner that maximizes reversibility.

METHODS

Cell fabrication

Battery-grade graphite (SLC1506T, Superior Graphite) was used as the active anode material in this work. Anodes were prepared using a pilot-scale processing facility at the University of Michigan Battery Lab. The prepared graphite anode is composed of 94% active material, 1% C65 conductive additive, and 5% CMC/SBR binder. An areal mass loading of 9.4 mg cm^{-2} (3.2 mAh cm^{-2} capacity loading) was controlled with a calendered porosity of $\sim 30\%$. $75 \text{ }\mu\text{m}$ thick Li metal foil (Alfa Aesar) was used to prepare the CE and RE for the visualization cell. Prior to cell assembly, the two surfaces of the Li foil were scraped to remove the native surface layers. 1 M LiPF_6 in 3:7 (w) EC:EMC electrolyte (Soulbrain) was used for all experiments in this work. $25 \text{ }\mu\text{m}$ thick PP/PE/PP separator was used for the CR2032 coin cells. $12 \text{ }\mu\text{m}$ thick PP/PE/PP separator was used for the pouch cells. For the pouch cells, $\text{LiNi}_{0.5}\text{Mn}_{0.3}\text{Co}_{0.2}\text{O}_2$ (battery grade, NMC-532, Toda America) was used as the cathode material. The cathode formulation was 92 wt.% NMC-532, 4 wt.% C65 conductive additive, and 4 wt.% PVDF binder. The cathode slurry was cast onto aluminum foils ($15 \text{ }\mu\text{m}$ thick) with a total areal mass loading of 16.58 mg/cm^2 and then calendered to 35% porosity. The visualization cell and the coin cells were assembled in an Ar glove box with H_2O and O_2 less than 0.5ppm. Pouch cells were assembled in a dry room (dew point of $< -40 \text{ }^\circ\text{C}$).

Electrochemical cycling

Prior to the fast charge experiments, the fully assembled visualization cells were rested at OCV for 4 hours and then pre-conditioned with two C/5 cycles using voltage cutoffs at 0.02 V and 0.4 V. For all of the visualization cell experiments, 2.7 mA/cm^2 is defined as 1C current. The visualization cells were cycled using a Biologic SP-200 or a Biologic VSP potentiostat. The coin cells were cycled on a Landt 2001a battery testing system. Pouch cells were cycled in a temperature-controlled chamber at $30 \text{ }^\circ\text{C}$ using a Maccor 4000 series automated test system (Maccor Inc.).

Visualization approach

Photographs of the electrode (**Fig. 1**) were taken using a UI-3080SE-C-HQ camera from Imaging Development Systems GmbH. Microscope images were taken using a Keyence VHS-700 digital

microscope. When Li plating occurred, the dendritic structure of the plated Li extended above the surface of the graphite electrode. To maintain both the plated Li and graphite surface in focus, focus variation microscopy was applied to extend the depth of focus of the images³⁵. The C/10 lithiation (**Fig. 2**) was recorded at a rate of 60 s/frame. The other visualization cell experiments were recorded at a rate of 15 s/frame to 20 s/frame. Data analysis, differential voltage and voltage-image synchronization were performed using MATLAB.

Coin cell disassembling

To create the cross sections of the coin cells in **Fig. 7**, CR2032 coin cells were disassembled with an MTI MSK-110 hydraulic crimper inside an Ar glovebox (O_2 and $H_2O < 0.5$ ppm). The graphite electrode was immediately retrieved and rinsed with dimethyl carbonate (DMC) to remove excess electrolyte. The disassembling and the rinsing process took less than 1min in total. The electrodes were then imaged by a Keyence VHS-700 digital microscope inside the Ar glovebox. For the electrodes shown in **Fig. 7**, the images were taken within 20min after disassembling.

ASSOCIATED CONTENT

Supporting Information.

The following files are available free of charge.

Supporting Information; (PDF)

AUTHOR INFORMATION

Corresponding Author

*Email: ndasgupt@umich.edu

ACKNOWLEDGMENT

The authors acknowledge support from the Office of Energy Efficiency and Renewable Energy (EERE) of the U.S. Department of Energy, under Award Number DE-EE0008362. This research was supported by a Bosch Energy Research Network (BERN) grant. Y.C. acknowledges support from a Phillips66 fellowship. This work was performed in part at the University of Michigan Battery Lab, and the authors would like to thank Greg Less, Joseph Gallegos, William Hicks, and Arthur Sinclair for their assistance on the pouch cell fabrication.

REFERENCES

- (1) Zeng, X.; Li, M.; Abd El-Hady, D.; Alshitari, W.; Al-Bogami, A. S.; Lu, J.; Amine, K. Commercialization of Lithium Battery Technologies for Electric Vehicles. *Adv. Energy Mater.* **2019**, *9* (27). <https://doi.org/10.1002/aenm.201900161>.
- (2) Gallagher, K. G.; Trask, S. E.; Bauer, C.; Woehrle, T.; Lux, S. F.; Tschech, M.; Lamp, P.; Polzin, B. J.; Ha, S.; Long, B.; Wu, Q.; Lu, W.; Dees, D. W.; Jansen, A. N. Optimizing Areal Capacities through Understanding the Limitations of Lithium-Ion Electrodes. *J. Electrochem. Soc.* **2016**, *163* (2), A138–A149. <https://doi.org/10.1149/2.0321602jes>.
- (3) Dahn, J. R. Phase Diagram of Li_xC_6 . *Phys. Rev. B* **1991**, *44* (17), 9170–9177. <https://doi.org/10.1103/PhysRevB.44.9170>.
- (4) Liu, Y.; Zhu, Y.; Cui, Y. Challenges and Opportunities towards Fast-Charging Battery Materials. *Nature Energy*. 2019, pp 540–550. <https://doi.org/10.1038/s41560-019-0405-3>.
- (5) Waldmann, T.; Hogg, B.-I. I.; Wohlfahrt-Mehrens, M. Li Plating as Unwanted Side Reaction in Commercial Li-Ion Cells – A Review. *J. Power Sources* **2018**, *384* (February), 107–124. <https://doi.org/10.1016/j.jpowsour.2018.02.063>.
- (6) Ng, B.; Coman, P. T.; Faegh, E.; Peng, X.; Karakalos, S. G.; Jin, X.; Mustain, W. E.; White, R. E. Low-Temperature Lithium Plating/Corrosion Hazard in Lithium-Ion Batteries: Electrode Rippling,

- Variable States of Charge, and Thermal and Nonthermal Runaway. *ACS Appl. Energy Mater.* **2020**. <https://doi.org/10.1021/acsaem.0c00130>.
- (7) Wandt, J.; Jakes, P.; Granwehr, J.; Eichel, R. A.; Gasteiger, H. A. Quantitative and Time-Resolved Detection of Lithium Plating on Graphite Anodes in Lithium Ion Batteries. *Mater. Today* **2018**, *21* (3), 231–240. <https://doi.org/10.1016/j.mattod.2017.11.001>.
- (8) Uhlmann, C.; Illig, J.; Ender, M.; Schuster, R.; Ivers-Tiffée, E. In Situ Detection of Lithium Metal Plating on Graphite in Experimental Cells. *J. Power Sources* **2015**, *279*, 428–438. <https://doi.org/10.1016/j.jpowsour.2015.01.046>.
- (9) Zinth, V.; Von Lüders, C.; Hofmann, M.; Hattendorff, J.; Buchberger, I.; Erhard, S.; Rebelo-Kornmeier, J.; Jossen, A.; Gilles, R. Lithium Plating in Lithium-Ion Batteries at Sub-Ambient Temperatures Investigated by in Situ Neutron Diffraction. *J. Power Sources* **2014**, *271*, 152–159. <https://doi.org/10.1016/j.jpowsour.2014.07.168>.
- (10) Guo, Z.; Zhu, J.; Feng, J.; Du, S. Direct in Situ Observation and Explanation of Lithium Dendrite of Commercial Graphite Electrodes. *RSC Adv.* **2015**, *5* (85), 69514–69521. <https://doi.org/10.1039/c5ra13289d>.
- (11) von Lüders, C.; Zinth, V.; Erhard, S. V.; Osswald, P. J.; Hofmann, M.; Gilles, R.; Jossen, A. Lithium Plating in Lithium-Ion Batteries Investigated by Voltage Relaxation and in Situ Neutron Diffraction. *J. Power Sources* **2017**, *342*, 17–23. <https://doi.org/10.1016/j.jpowsour.2016.12.032>.
- (12) Gotoh, K.; Izuka, M.; Arai, J.; Okada, Y.; Sugiyama, T.; Takeda, K.; Ishida, H. In Situ ⁷Li Nuclear Magnetic Resonance Study of the Relaxation Effect in Practical Lithium Ion Batteries. *Carbon N. Y.* **2014**, *79* (1), 380–387. <https://doi.org/10.1016/j.carbon.2014.07.080>.
- (13) Arai, J.; Okada, Y.; Sugiyama, T.; Izuka, M.; Gotoh, K.; Takeda, K. In Situ Solid State ⁷Li NMR Observations of Lithium Metal Deposition during Overcharge in Lithium Ion Batteries. *J.*

- Electrochem. Soc.* **2015**, *162* (6), A952–A958. <https://doi.org/10.1149/2.0411506jes>.
- (14) Märker, K.; Xu, C.; Grey, C. P. Operando NMR of NMC811/Graphite Lithium-Ion Batteries: Structure, Dynamics, and Lithium Metal Deposition. *J. Am. Chem. Soc.* **2020**. <https://doi.org/10.1021/jacs.0c06727>.
- (15) Gotoh, K.; Yamakami, T.; Nishimura, I.; Kometani, H.; Ando, H.; Hashi, K.; Shimizu, T.; Ishida, H. Mechanisms for Overcharging of Carbon Electrodes in Lithium-Ion/Sodium-Ion Batteries Analysed by Operando Solid-State NMR †. *J. Mater. Chem. A* **2020**. <https://doi.org/10.1039/d0ta04005c>.
- (16) Finegan, D. P.; Quinn, A.; Wragg, D. S.; Colclasure, A. M.; Lu, X.; Tan, C.; Heenan, T. M. M.; Jervis, R.; Brett, D. J. L.; Das, S.; Gao, T.; Cogswell, D. A.; Bazant, M. Z.; Di Michiel, M.; Checchia, S.; Shearing, P. R.; Smith, K. Spatial Dynamics of Lithiation and Lithium Plating during High-Rate Operation of Graphite Electrodes. *Energy Environ. Sci.* **2020**, *13* (8), 2570–2584. <https://doi.org/10.1039/d0ee01191f>.
- (17) Gao, T.; Han, Y.; Fraggedakis, D.; Das, S.; Zhou, T.; Yeh, C.; Xu, S.; Chueh, W. C.; Li, J.; Bazant, M. Z. Interplay of Lithium Intercalation and Plating on a Single Graphite Particle. *Joule* **2021**, *5*, 1–22. <https://doi.org/10.1016/j.joule.2020.12.020>.
- (18) McShane, E. J.; McShane, E. J.; Colclasure, A. M.; Brown, D. E.; Brown, D. E.; Konz, Z. M.; Konz, Z. M.; Smith, K.; McCloskey, B. D.; McCloskey, B. D. Quantification of Inactive Lithium and Solid-Electrolyte Interphase Species on Graphite Electrodes after Fast Charging. *ACS Energy Lett.* **2020**, *5* (6), 2045–2051. <https://doi.org/10.1021/acseenergylett.0c00859>.
- (19) Bommier, C.; Chang, W.; Lu, Y.; Yeung, J.; Davies, G.; Mohr, R.; Williams, M.; Steingart, D. In Operando Acoustic Detection of Lithium Metal Plating in Commercial LiCoO₂/Graphite Pouch Cells. *Cell Reports Phys. Sci.* **2020**, 100035. <https://doi.org/10.1016/j.xcrp.2020.100035>.

- (20) Krachkovskiy, S. A.; Reza, M.; Aguilera, A. R.; Halalay, I. C.; Balcom, B. J.; Goward, G. R. Real-Time Quantitative Detection of Lithium Plating by In Situ NMR Using a Parallel-Plate Resonator. *J. Electrochem. Soc.* **2020**, *167* (13), 130514. <https://doi.org/10.1149/1945-7111/abb7ea>.
- (21) Fear, C.; Adhikary, T.; Carter, R.; Mistry, A. N.; Love, C. T.; Mukherjee, P. P. In Operando Detection of the Onset and Mapping of Lithium Plating Regimes during Fast Charging of Lithium-Ion Batteries. *ACS Appl. Mater. Interfaces* **2020**, *12* (27), 30438–30448. <https://doi.org/10.1021/acsami.0c07803>.
- (22) Harris, S. J.; Timmons, A.; Baker, D. R.; Monroe, C. Direct in Situ Measurements of Li Transport in Li-Ion Battery Negative Electrodes. *Chem. Phys. Lett.* **2010**, *485* (4–6), 265–274. <https://doi.org/10.1016/j.cplett.2009.12.033>.
- (23) Sun, F.; He, X.; Jiang, X.; Osenberg, M.; Li, J.; Zhou, D.; Dong, K.; Hilger, A.; Zhu, X.; Gao, R.; et al. Advancing Knowledge of Electrochemically Generated Lithium Microstructure and Performance Decay of Lithium Ion Battery by Synchrotron X-Ray Tomography. *Mater. Today* **2018**, *27*, 21–32. <https://doi.org/10.1016/j.mattod.2018.11.003>.
- (24) Tanim, T. R.; Paul, P. P.; Thampy, V.; Cao, C.; Steinrück, H.-G.; Nelson Weker, J.; Toney, M. F.; Dufek, E. J.; Evans, M. C.; Jansen, A. N.; Polzin, B. J.; Dunlop, A. R.; Trask, S. E. Heterogeneous Behavior of Lithium Plating during Extreme Fast Charging. *Cell Reports Phys. Sci.* **2020**, *1* (7), 100114. <https://doi.org/10.1016/j.xcrp.2020.100114>.
- (25) Jin, Y.; Zheng, Z.; Wei, D.; Jiang, X.; Lu, H.; Sun, L.; Tao, F.; Guo, D.; Liu, Y.; Gao, J.; Cui, Y. Detection of Micro-Scale Li Dendrite via H₂ Gas Capture for Early Safety Warning. *Joule* **2020**, *4* (8), 1714–1729. <https://doi.org/10.1016/j.joule.2020.05.016>.
- (26) Burns, J. C.; Stevens, D. A.; Dahn, J. R. In-Situ Detection of Lithium Plating Using High Precision Coulometry. *J. Electrochem. Soc.* **2015**, *162* (6), A959–A964. <https://doi.org/10.1149/2.0621506jes>.

- (27) Rangarajan, S. P.; Barsukov, Y.; Mukherjee, P. P. In Operando Signature and Quantification of Lithium Plating. *J. Mater. Chem. A* **2019**, *7* (36), 20683–20695.
<https://doi.org/10.1039/c9ta07314k>.
- (28) Petzl, M.; Kasper, M.; Danzer, M. A. Lithium Plating in a Commercial Lithium-Ion Battery e A Low-Temperature Aging Study. *J. Power Sources* **2015**, *275*, 799–807.
<https://doi.org/10.1016/j.jpowsour.2014.11.065>.
- (29) Petzl, M.; Danzer, M. A. Nondestructive Detection, Characterization, and Quantification of Lithium Plating in Commercial Lithium-Ion Batteries. *J. Power Sources* **2014**, *254*, 80–87.
<https://doi.org/10.1016/j.jpowsour.2013.12.060>.
- (30) Schindler, S.; Bauer, M.; Petzl, M.; Danzer, M. A. Voltage Relaxation and Impedance Spectroscopy as In-Operando Methods for the Detection of Lithium Plating on Graphitic Anodes in Commercial Lithium-Ion Cells. *J. Power Sources* **2016**, *304*, 170–180.
<https://doi.org/10.1016/j.jpowsour.2015.11.044>.
- (31) Campbell, I. D.; Marzook, M.; Marinescu, M.; Offer, G. J. How Observable Is Lithium Plating? Differential Voltage Analysis to Identify and Quantify Lithium Plating Following Fast Charging of Cold Lithium-Ion Batteries. *J. Electrochem. Soc.* **2019**, *166* (4), A725–A739.
<https://doi.org/10.1149/2.0821904jes>.
- (32) Konz, Z. M.; Mcshane, E. J.; Mccloskey, B. D. Detecting the Onset of Lithium Plating and Monitoring Fast Charging Performance with Voltage Relaxation. *ACS Energy Lett* **2020**, *22*, 54.
<https://doi.org/10.1021/acseenergylett.0c00831>.
- (33) Carter, R.; Parker, J. F.; Wolak, M. A.; Love, C. T.; Sassin, M. B.; Klein, E. J.; Long, J. W. Initiated Chemical Vapor Deposition of Ultrathin Polymer Coatings at Graphite Electrodes for Enhanced Performance in Li-Ion Batteries Initiated Chemical Vapor Deposition of Ultrathin Polymer Coatings at Graphite Electrodes for Enhanced Performance in Li-I. *J. Electrochem. Soc.*

- 2020**, *167*. <https://doi.org/10.1149/1945-7111/ab7f22>.
- (34) Sanchez, A. J.; Kazyak, E.; Chen, Y.; Chen, K. H.; Pattison, E. R.; Dasgupta, N. P. Plan-View Operando Video Microscopy of Li Metal Anodes: Identifying the Coupled Relationships among Nucleation, Morphology, and Reversibility. *ACS Energy Lett.* **2020**, *5* (3), 994–1004. <https://doi.org/10.1021/acseenergylett.0c00215>.
- (35) Sanchez, A. J.; Kazyak, E.; Chen, Y.; Lasso, J.; Dasgupta, N. P. Lithium Stripping: Anisotropic Evolution and Faceting of Pits Revealed by Operando 3-D Microscopy. *J. Mater. Chem. A* **2021**. <https://doi.org/10.1039/D1TA03333F>.
- (36) Chen, K. H.; Namkoong, M. J.; Goel, V.; Yang, C.; Kazemiabnavi, S.; Mortuza, S. M.; Kazyak, E.; Mazumder, J.; Thornton, K.; Sakamoto, J.; Dasgupta, N. P. Efficient Fast-Charging of Lithium-Ion Batteries Enabled by Laser-Patterned Three-Dimensional Graphite Anode Architectures. *J. Power Sources* **2020**, *471*, 228475. <https://doi.org/10.1016/j.jpowsour.2020.228475>.
- (37) Chen, K. H.; Goel, V.; Namkoong, M. J.; Wied, M.; Müller, S.; Wood, V.; Sakamoto, J.; Thornton, K.; Dasgupta, N. P. Enabling 6C Fast Charging of Li-Ion Batteries with Graphite/Hard Carbon Hybrid Anodes. *Adv. Energy Mater.* **2020**, *11*, 200336. <https://doi.org/10.1002/aenm.202003336>.
- (38) Maire, P.; Evans, A.; Kaiser, H.; Scheifele, W.; Novák, P. Colorimetric Determination of Lithium Content in Electrodes of Lithium-Ion Batteries. *J. Electrochem. Soc.* **2008**, *155* (11), 862–865. <https://doi.org/10.1149/1.2979696>.
- (39) Grimsmann, F.; Gerbert, T.; Brauchle, F.; Gruhle, A.; Parisi, J.; Knipper, M. Hysteresis and Current Dependence of the Graphite Anode Color in a Lithium-Ion Cell and Analysis of Lithium Plating at the Cell Edge. *J. Energy Storage* **2018**, *15*, 17–22. <https://doi.org/10.1016/j.est.2017.10.015>.

- (40) Basu, S.; Zeller, C.; Flanders, P. J.; Fuerst, C. D.; Johnson, W. D.; Fischer, J. E. Synthesis and Properties of Lithium-Graphite Intercalation Compounds. *Mater. Sci. Eng.* **1979**, *38* (3), 275–283. [https://doi.org/10.1016/0025-5416\(79\)90132-0](https://doi.org/10.1016/0025-5416(79)90132-0).
- (41) Dresselhaus, M. S.; Dresselhaus, G. Intercalation Compounds of Graphite. *Adv. Phys.* **2002**, *51* (1), 1–186. <https://doi.org/10.1080/00018730110113644>.
- (42) Harris, S. J.; Lu, P. Effects of Inhomogeneities -Nanoscale to Mesoscale -on the Durability of Li-Ion Batteries. *J. Phys. Chem. C* **2013**, *117* (13), 6481–6492. <https://doi.org/10.1021/jp311431z>.
- (43) Persson, K.; Sethuraman, V. A.; Hardwick, L. J.; Hinuma, Y.; Meng, Y. S.; Van Der Ven, A.; Srinivasan, V.; Kostecki, R.; Ceder, G. Lithium Diffusion in Graphitic Carbon. *J. Phys. Chem. Lett* **2010**, *1*, 1176–1180. <https://doi.org/10.1021/jz100188d>.
- (44) Harris, S. J.; Rahani, E. K.; Shenoy, V. B. Direct In Situ Observation and Numerical Simulations of Non-Shrinking-Core Behavior in an MCMB Graphite Composite Electrode. *J. Electrochem. Soc.* **2012**, *159* (9), A1501–A1507. <https://doi.org/10.1149/2.055209jes>.
- (45) Wood, K. N.; Kazyak, E.; Chadwick, A. F.; Chen, K. H.; Zhang, J. G.; Thornton, K.; Dasgupta, N. P. Dendrites and Pits: Untangling the Complex Behavior of Lithium Metal Anodes through Operando Video Microscopy. *ACS Cent. Sci.* **2016**, *2* (11), 790–801. <https://doi.org/10.1021/acscentsci.6b00260>.
- (46) Chen, K. H.; Wood, K. N.; Kazyak, E.; Lepage, W. S.; Davis, A. L.; Sanchez, A. J.; Dasgupta, N. P. Dead Lithium: Mass Transport Effects on Voltage, Capacity, and Failure of Lithium Metal Anodes. *J. Mater. Chem. A* **2017**, *5* (23), 11671–11681. <https://doi.org/10.1039/c7ta00371d>.
- (47) Peled, E. The Electrochemical Behavior of Alkali and Alkaline Earth Metals in Nonaqueous Battery Systems—The Solid Electrolyte Interphase Model. *J. Electrochem. Soc.* **1979**, *126* (12), 2047–2051. <https://doi.org/10.1149/1.2128859>.

- (48) Yang, X. G.; Ge, S.; Liu, T.; Leng, Y.; Wang, C. Y. A Look into the Voltage Plateau Signal for Detection and Quantification of Lithium Plating in Lithium-Ion Cells. *J. Power Sources* **2018**, *395* (April), 251–261. <https://doi.org/10.1016/j.jpowsour.2018.05.073>.
- (49) LePage, W. S.; Chen, Y.; Kazyak, E.; Chen, K.-H.; Sanchez, A. J.; Poli, A.; Arruda, E. M.; Thouless, M. D.; Dasgupta, N. P. Lithium Mechanics: Roles of Strain Rate and Temperature and Implications for Lithium Metal Batteries. *J. Electrochem. Soc.* **2019**, *166* (2), A89–A97. <https://doi.org/10.1149/2.0221902jes>.
- (50) Hogrefe, C.; Hein, S.; Waldmann, T.; Danner, T.; Richter, K.; Latz, A.; Wohlfahrt-Mehrens, M. Mechanistic Details of the Spontaneous Intercalation of Li Metal into Graphite Electrodes. *J. Electrochem. Soc.* **2020**, *167* (14), 140546. <https://doi.org/10.1149/1945-7111/abc8c3>.
- (51) O’Kane, S. E. J.; Campbell, I. D.; Marzook, M. W. J.; Offer, G. J.; Marinescu, M. Physical Origin of the Differential Voltage Minimum Associated with Lithium Plating in Li-Ion Batteries. *J. Electrochem. Soc.* **2020**, *167* (9), 090540. <https://doi.org/10.1149/1945-7111/ab90ac>.
- (52) Bauer, M.; Rieger, B.; Schindler, S.; Keil, P.; Wachtler, M.; Danzer, M. A.; Jossen, A. Multi-Phase Formation Induced by Kinetic Limitations in Graphite-Based Lithium-Ion Cells: Analyzing the Effects on Dilation and Voltage Response. *J. Energy Storage* **2017**, *10*, 1–10. <https://doi.org/10.1016/j.est.2016.11.006>.